

This is the accepted manuscript made available via CHORUS. The article has been published as:

Quantum confinement and anisotropy in thin-film molecular semiconductors

Eric A. Muller, James E. Johns, Benjamin W. Caplins, and Charles B. Harris

Phys. Rev. B **83**, 165422 — Published 14 April 2011

DOI: [10.1103/PhysRevB.83.165422](https://doi.org/10.1103/PhysRevB.83.165422)

Quantum Confinement and Anisotropy in Thin Film Molecular Semiconductors

Eric A. Muller, James E. Johns, Benjamin W. Caplins, and Charles B. Harris

*Department of Chemistry, University of California Berkeley
Berkeley, CA 94720*

(Dated: February 11, 2011)

Unoccupied electronic states are probed in epitaxial films of metal phthalocyanines on Ag(111), using angle-resolved two photon photoemission spectroscopy. Quantum confinement of an image state wavefunction results in band folding and the opening of a band gap. Angle resolve photoemission intensity measurements resolve the probability density of the wavefunction, and are able to identify the symmetry of each band. These results are compared with predictions from a 2-dimensional scattering model, and they point to the importance of the spatial extent and symmetry of functional groups in predicting and controlling electronic structure on surfaces and in molecular thin films.

PACS numbers: 73.20.At, 79.60.-i, 79.60.Jv

REVIEW COPY
NOT FOR DISTRIBUTION

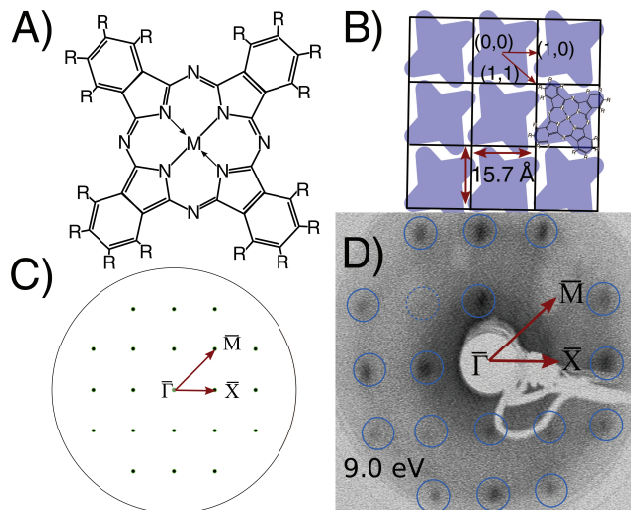


FIG. 1. A): Phthalocyanine structure. $M = \text{Fe}$ or Cu ; $R = \text{H}$. B): Schematic of phthalocyanine lattice showing high symmetry directions. C) Predicted LEED for FePc/Ag(111). D) Experimental LEED for FePc/Ag(111).

Much of the behavior in electronic devices and heterogeneous catalysts is defined by the energy level alignment, band structure, and spatial extent of electrons at the interface between two materials^{1–3}. Much experimental success has been made recently in controlling and confining occupied surface state electrons using single atomic defects, quantum corrals and periodic nanoporous lattices on metal surfaces^{4,5}. Nanometer unit cell sizes approaching the Fermi wavelength allows direct modification of surface states with these scattering barriers.

Scattering models have had much success describing these surface modifications^{6,7}. Although atomistic and *ab initio* descriptions would be ideal, nanometer unit cells at a surface are prohibitively large to calculate, and DFT approaches do not properly treat unoccupied states^{8,9}. Instead, scattering models are computationally inexpensive and can be fit to with empirically derived model potentials³. Further, the analogy between a corral or porous lattice and scattering barriers makes such descriptions physically intuitive.

In this work, we probe unoccupied electronic band structure in molecular thin films with photoemission spectroscopy, and we demonstrate that our results can be understood through similar scattering models. In a molecular film, the potential energy surfaces presented by different functional groups act as the quantum wells and scattering barriers experienced by an injected electron. Molecular semiconductors consist mainly of delocalized π - and π^* -orbitals interrupted by localized and directional σ -orbitals at the molecule edges, of which the latter acts as our scattering lattice. Building off the potential energy surfaces introduced by Kronig and Penney¹⁰, we introduce a 2D model pseudopotential that is able to predict band folding, symmetry, and spatial extent of unoccupied surface electrons using only the symmetry and spatial extent of functional groups within the unit cell. These results compare well with our experimental observations. Our results highlight the importance of intermolecular coupling and symmetry in controlling band properties.

We report photoemission experiments of an injected electron in a crystalline monolayer film of metal-phthalocyanine (MPc). MPc's have been shown to achieve high efficiencies in molecular electronic devices¹¹, and as a result are increasingly studied as model molecules. Copper- and iron- phthalocyanines (CuPc and FePc), depicted in Figure 1A, were epitaxially grown on an atomically smooth surface of Ag(111), prepared by (Ar^+) sputtering and annealing. Ordered layers were grown epitaxially on a Ag substrate held at 300K ^{12,13}. In agreement with previous literature reports, a highly ordered and uniform single molecular layer formed after annealing a multilayer film up to 580K for 30 minutes followed by cooling to a base temperature of 130K ¹⁴. This annealing process removed any evidence of second or higher monolayer coverages.

Low Energy Electron Diffraction (LEED) shows that both CuPc and FePc grow epitaxially in a square lattice, with a single molecule per unit cell and a repeat distance comparable to the literature value of $15 - 16 \text{ \AA}$, (Figure 1)^{15–17}. CuPc and FePc differ slightly in packing as a result of the symmetry of the substrate. Epitaxial growth on the six-fold symmetric Ag(111) substrate causes the CuPc to pack into 12 different domains rotated by 30° with respect to one another¹⁸. The FePc, however, packs as a single square lattice, while the other rotated domains are unobserved. The presence of only a single oriented domain in FePc may result from residual step edges growing laterally on the Ag(111) substrate^{17,19}.

Angle- and time-resolved two photon photoemission spectroscopy (TPPE) is used to investigate the unoccupied electronic states in each system. In this technique, a femtosecond pump pulse excites an electron from below the Fermi level of the metal and into a previously unoccupied state. After a waiting time, a second, probe pulse photoemits the electron into a time-of-flight energy detector.

Angle dependent measurements resolve the electronic momentum, picking out solid angles of acceptance by rotating the sample with respect to a detector behind a slit, in a manner similar to one-photon angle resolve photoemission

spectroscopy (ARPES). The angle, θ , and momentum parallel to the surface, $k_{||}$, of the photoemitted electron are related by the measured energy $E_{\text{photoemitted}}$ and the mass, m_e , of an electron:

$$k_{||} = \sqrt{\frac{2 \cdot m_e \cdot E_{\text{photoemitted}}}{\hbar^2}} \cdot \sin(\theta) \quad (1)$$

The energy versus momentum dispersion relation characterizes the band structure and coupling in a material.

Momentum dependent intensities have been previously shown to be related to the square modulus of the initial and final states, $(\Psi_i \text{ and } \Psi_f)$, coupled by the electromagnetic vector potential and electron momentum operators^{20,21}:

$$I \propto |\langle \Psi_i(x, y) | \hat{A} \cdot \hat{p}_z | \Psi_f(x, y) \rangle|^2 \quad (2)$$

The photoemitted intensity, I , measured at different angles, thus relates directly to the initial state k-space wavefunction by a simple transformation. ARPES experiments have observed k-space intensity fluctuations resulting from fourier transformed real space molecular orbitals²². Similarly, angle-resolved TPPE experiments have related gaussian intensity distributions to localized, trapped electronic wavefunctions²³.

Here, an image potential state (IPS) electron probes potential energy corrugation in the MPc adlayer. Briefly, an IPS occurs when an electron ejected outside a metal surface induces a reorganization of charge inside the metal. On clean, high symmetry noble metal surfaces, a Rydberg series of bound states form, which remain delocalized parallel to the surface²⁴. The $n=1$ IPS resides within the first few Å outside a bare metal or metal with an adlayer of attractive electron affinity. The IPS electron is thus an ideal probe of the first few adsorbed monolayers.

Three IPS are seen for monolayer coverages of both FePc/Ag(111) and CuPc/Ag(111). IPS binding energies are measured at -0.85eV , -0.55eV and -0.14eV in FePc, and at -0.90eV , -0.60eV and -0.19eV in CuPc, relative to the vacuum level (Figure 2A)¹⁸. The workfunctions, measured to be $4.15 \pm 0.1\text{ eV}$ by the high and low energy photoemission cutoffs and the onset of one photon photoemission, places the observed energy levels in FePc and CuPc within instrumental error of one another. These states do not fit to the typical image state Rydberg progression. Further, the binding energy of the lowest state is below that of clean Ag(111), suggesting IPS mixing with one or more of the phthalocyanine LUMO of attractive electron affinity. The presence of multiple low lying LUMO states supports such a hybridization but prevent assignment to mixing with a single orbital²⁵. Lifetimes, measured to be $30 \pm 15\text{ fs}$ in all three peaks, determined with a pump-probe cross correlation of 100 fs, are also consistent with a LUMO hybridization. We introduce the progression of states here as $j = (1, 1)$, $j = (2, 1)$, and $j = (3, 1), (1, 3)$ backfolded bands of the $n=1$ IPS, as will be discussed below.

The dispersion of FePc was probed along the $\bar{\Gamma}-\bar{X}$ direction as determined by LEED, while the CuPc dispersion was averaged across different directions resulting from the additional rotated lattice domains. These three image states have both positive and negative effective masses, measured to be 1.5, -2.0 and $1.1\ m_e$ for the $j=(1, 1)$, $(2, 1)$ and $(3, 1), (1, 3)$ states in FePc. While the small effective masses imply delocalization, the negative effective mass of the $j = (2, 1)$ is unusual for a free-electron-like image state, implying significant interaction with the MPc lattice. Further, the $j = (1, 1)$ and $j = (2, 1)$ states have energetic minima and maxima at $0.21 \pm 0.03\text{ \AA}^{-1}$, which corresponds well to Brillouin zone folding with the periodicity of the MPc.

Lastly, sharp variation in photoemission intensity as a function of parallel momentum is observed. The $j = (1, 1)$ and $j = (3, 1), (1, 3)$ bands have maximum intensity near the $\bar{\Gamma}$ point, while $j = (2, 1)$ has a maximum intensity at the \bar{X} point of the adlayer, (Figures 3A and 3B). Momentum dependent intensities thus distinguish these hybridized IPS from free electrons, yet do not match molecular orbital descriptions, and new modeling is merited.

We model these results beginning with the square well potential originally discussed by Kronig and Penney¹⁰. A similar 1D model has successfully described photoemission intensity scattering on stepped metal surfaces²⁶. Here, however, our potential energy corrugation results from the image electron coupling with different functional groups across the surface. The image electron couples with the aromatic core of the MPc, which acts as a smooth, attractive potential within the center of each molecule. This delocalized core, however extends only $12 - 13\text{ \AA}$ across the $15 - 16\text{ \AA}$ unit cell. The remaining 3 \AA at the unit cell edges contains C-H bonds. Unlike the aromatic, π^* core, σ -orbitals along the C-H bonds are both directional and localized. Further, the lowest unoccupied (σ^*) orbitals residing on the C-H bonds are much higher in energy than the π^* LUMO orbitals. Interaction with the repulsive σ^* orbitals can thus be approximated by a higher effective potential energy surface in this region.

Considering these two components in constructing a pseudopotential, the σ^* orbitals act as a scattering barrier at the edge of the MPc, modeled as a potential step. The barrier height and width are the only adjustable parameters of the model, the latter of which was set to the approximate width of the C-H bonds. The barrier height was empirically set to 0.5 eV to obtain a best fit of energies near the $\bar{\Gamma}$ point. This energetic height is intermediate between the smaller, $0.1\text{--}0.25\text{ eV}$, barriers that have been used to model the occupied surface state confined in nanoporous superlattices and the larger potential energy that could be expected from an unscreened interaction with the σ^* orbital²⁷. This intermediate empirical value is consistent with qualitative expectations for an image electron, which has more electron density within the layer than a surface state electron, while still having electron density in both the metal and vacuum.

Separation of variables allows the scattering parallel to the surface to be treated independently from binding normal to the surface. This simple Kronig-Penney model thus only explicitly treats the 2D potential parallel to the

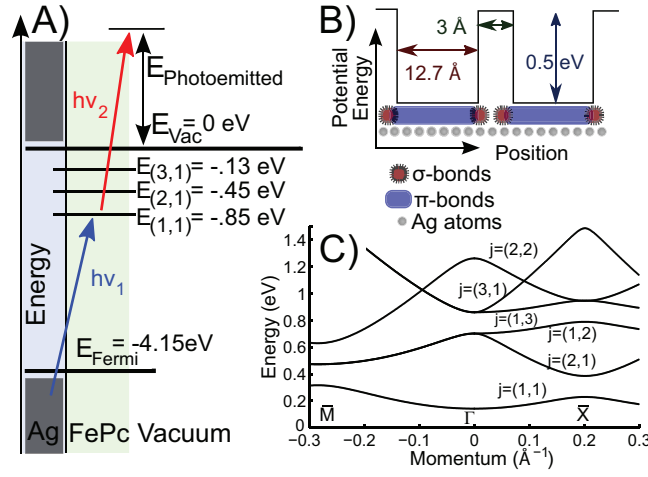


FIG. 2. Schematic of TPPE. A pump pulse excites an electron from the Ag (light blue) into the FePc adlayer (light green) before photoemission. Energies are referenced to the vacuum level. B): Cut through of the modeled potential energy surface showing a series of quantum wells parallel to the surface. C): Band structure of the lowest several states, calculated along high symmetry directions.

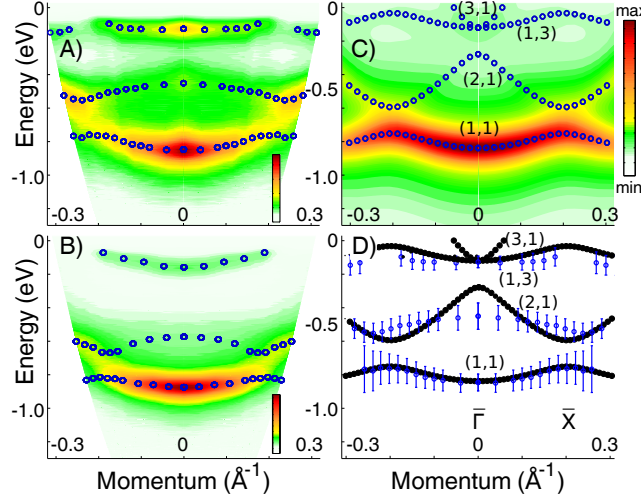


FIG. 3. Experimental band structure and photoemission intensity for FePc (A), CuPc (B), and predicted photoemission for FePc (C). Peak centers shown with blue circles. (D) Comparison between predicted observable band structure (black) and experimental peak fits (blue) with error bars 1/4 FWHM of the fit.

surface and assumes a bound state normal to the surface. Energies are obtained by finding the determinates of the Schrödinger equation¹⁸:

$$(V_{\vec{x}} + V_{\vec{y}} - E)(\psi_{\vec{x},\vec{y}}) = \frac{\hbar^2}{2m_e} \nabla_x^2 \nabla_y^2 (\psi_{\vec{x},\vec{y}}) \quad (3)$$

Here m_e is the mass of the electron, and $\psi_{\vec{x},\vec{y}} = (\psi_{\vec{x}}^0 \psi_{\vec{y}}^0 e^{i(\vec{k}_{x,y} \cdot \vec{r}_{x,y})})$ are the Bloch plane wave solutions. Solutions are calculated using the finite difference method and periodic boundary conditions²⁸. Eigenvalue energies, E , versus wave vector, $\vec{k}_{x,y}$, yield band dispersions. Each band, resulting from Brillouin zone folding, can be labeled in convention with the 2D quantum level nomenclature, where the quantum numbers, $j = (m, n)$, indicate the band folding in the k_x and k_y directions²⁹. Band dispersions of the lowest energy states, $j = (1, 1)$ through $j = (3, 1)$ and $(1, 3)$, are plotted in figure 2C along the $\bar{\Gamma}-\bar{X}$ and $\bar{\Gamma}-\bar{M}$ directions. The former corresponds to the experimentally probed direction in FePc, while $\bar{\Gamma}-\bar{M}$ represents a rotation of 45° to the corner of the Brillouin zone.

Finally, the k -space probability density is calculated in order to recreate the intensity distribution. Bloch wavefunctions are first calculated as real space eigenvectors of equation 3. Fourier transforming and multiplication by the complex conjugate results in a normalized 2-dimensional probability density in k -space. Band energy and intensity are then calculated along the $\bar{\Gamma}-\bar{X}$ direction to match the probed orientation in FePc.

The resulting predicted spectrum measures electron probability density as a function of energy and momentum (Figure 3C). Lifetime and inhomogeneous broadening in energy are represented as a 250 meV Voigt line-width. It is immediately apparent that fewer bands are observed here than exist in the full band structure (Figure 2C). Only

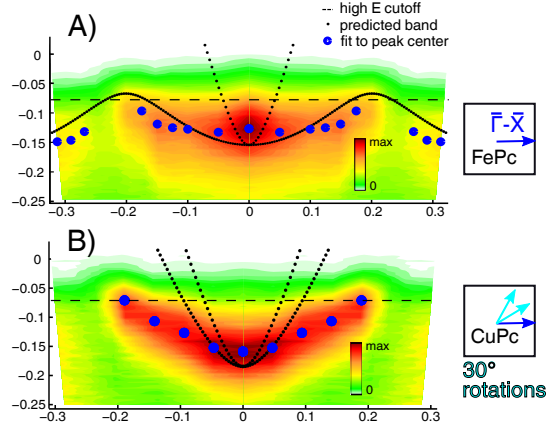


FIG. 4. Anisotropy results in different dispersions and for the $j=(1,3)$ and $(3,1)$ bands as seen experimentally in FePc (A), and CuPc (B). Modeling predicts the $j = (1,3)$ band to return below the HEC in FePc at high momenta (black dots), while it rises monotonically above the HEC in CuPc.

the $j = (1,1)$, $(2,1)$, $(1,3)$ and $(3,1)$ quantum levels contribute significant intensity to the observed spectrum, while the $j = (1,2)$ and $(2,2)$ states have minimal intensity along the directions and momenta probed.

Comparison between the modeled results and experimental spectra (Figure 3A-C) shows strong agreement. Three peaks are clearly visible in each spectra, arising from the $j = (1,1)$, $(2,1)$, $j = (1,3)$ and $(3,1)$ states. Intensities are observed as the square of the wavefunction probability density. Experimental intensities of the are strikingly similar to the 2D square well predictions, given the simplicity of the model. The $j = (1,1)$ and $(1,3)$ and $(3,1)$ states, predicted to be *gerade* by the symmetry of the square well, are observed as *gerade* states with maximum intensity near the $\bar{\Gamma}$ point. The $j = (2,1)$ state is predicted to be *ungerade* with one node at the $\bar{\Gamma}$ point, and experimentally has a single minimum at $\bar{\Gamma}$. The intensity does not fully reach zero at $\bar{\Gamma}$, which may be caused by finite angle resolution and broadening.

Finally, it is interesting to note that the relative intensities of observed bands relative to one another approximately match the intensities predicted by the normalized wavefunctions. In order for the final state photoemission intensities to match normalized predictions in the model, there must be near uniform occupancy of the backfolded band, and therefore similar excitation probabilities^{30,31}. The transition dipole for excitation from, and decay to the metal are both proportional to the extent of the wavefunction into the metal, and excitation and decay can be treated similarly²⁵. Previous experiments on IPS suggest that coupling to the metal is relatively uniform within a single band³². Here, where we have treated bandfolding of the $n=1$ IPS parallel to the surface, we expect uniform penetration into the bulk. Uniform transition dipole moments are thus expected, and this is supported by the similarly short decay times measured in each of the three peaks.

The $n=2$ IPS, which is not observed above the background in our experiment, is expected to have a smaller transition dipole. The $n=2$ IPS extends further into the vacuum and has less bulk penetration at a noble metal surface. This commonly results in longer $n=2$ lifetimes and peak intensities that may be smaller by two orders of magnitude^{33,34}. Although the lower intensity of the $n=2$ state is common to many systems, it is expected to be particularly true when both the $n=1$ and $n=2$ states are within the surface bandgap, as they are here due to the vacuum level shift and lowered workfunction.

Experimentally observed band dispersions for FePc are plotted in figure 3D against modeled predictions. States with predicted low intensity are omitted. The curvatures of the $j = (1,1)$ and $j = (3,1)$, $(1,3)$ states fit the model to well within experimental results. The $j = (2,1)$ state, however, has a bandwidth notably less than that of the model. Finite angular resolution at the detector contributes to the band narrowing. Band narrowing may also occur from finite temperature electron-phonon coupling, or potential energy corrugation unaccounted for in the coarse grained model³⁵.

Anisotropic dispersions distinguish between the FePc and CuPc films. While FePc is probed only along $\bar{\Gamma}-\bar{X}$, the CuPc dispersion is integrated over each rotated lattice domain. Summing calculations over angles rotated in 30° increments from $\bar{\Gamma}-\bar{X}$ mirrors the experimental integration over rotated domains. Modeling shows that the $j = (1,1)$ state is nearly isotropic within the probed region, and is similar between FePc and CuPc. The $j = (2,1)$ state varies greatly in bandwidth as a function of detection angle. The observed $j = (2,1)$ curvatures in FePc and CuPc are similar, however, because the $\bar{\Gamma}-\bar{X}$ direction, probed in both systems, contains greater intensity than the other rotated domains probed only in CuPc. As a result, the band curvature differs little, while the intensity of the $j = (2,1)$ state is decreased in intensity relative to $j = (1,1)$ in CuPc.

The $j = (1,3)$ state shows more striking anisotropy. Along the $\bar{\Gamma}-\bar{X}$ direction of FePc, this state briefly rises above the high energy cutoff (HEC) becoming unobservable at intermediate momenta, before curving back below the HEC at large momenta (Figure 4A). In CuPc, however, dispersions along the rotated domains rise monotonically above the HEC (Figure 4C). Rotated domains thus cause the $j = (1,3)$ intensity to decrease by a factor of 3 at high

momenta in CuPc, and peaks are not observable above background noise. Anisotropic dispersions are thus able to distinguish between multiple and single crystal orientations using only a single detection axis.

Our results demonstrate a simple way of predicting band curvature, photoemission intensity and anisotropy in molecular thin films. Much of the electronic structure can be understood solely in terms of the symmetry and the locations of σ and π -bonds within the unit cell.

The results discussed here contrast other work studying surface electronic states and molecular semiconductors. Much work in this field focuses on the energy levels of molecularly derived orbitals, referenced to the isolated molecule. Similarly, band width is often treated as simply a measure of the strength of intermolecular coupling, ignoring symmetry and spatial extent. Our work, on the other hand, suggests that symmetry and lattice size may in some cases play a dominant role in the observed electronic structure, controlling and tuning the anisotropic band splitting, quantum confinement, and wavefunctions.

We have developed here a simple and chemically intuitive picture of scattering and its effects on band structure in molecular crystals. While this type of lattice confinement is not expected to be observed for molecules or lattices <1 nm across, this type of band folding likely plays a role in defining the physical properties of a whole range of larger molecular and polymeric semiconductors, which are gaining ever more prominence in new devices.

Finally, these results directly examine a parameter for tuning charge carrier properties via lattice dimensions and the symmetry and extent of σ -bond scattering centers. Bands resulting from this type of scattering process will have altered mobility parallel to the surface, as well as charge injection and coupling across the interface. Further, the localization and symmetry of charge density will affect surface chemical bonding and orientation, both of which are important parameters in understanding catalytic processes.

ACKNOWLEDGMENTS

This work was supported by the Director, Office of Science, Office of Basic Energy Sciences, Chemical Sciences Division of the U.S. Department of Energy, under Contract No. DE-AC02-05CH11231. We acknowledge NSF support for specialized equipment used in the experiments herein.

-
- ¹ A. L. Linsebigler, G. Q. Lu, and J. T. Yates. Chem. Rev. **95**, 735 (1995).
- ² H. Ishii *et al.* Adv. Mat. **11**, 605 (1999).
- ³ F. Klappenberger *et al.* Phys. Rev. Lett. **106**, 026802 (2011).
- ⁴ M. F. Crommie, C. P. Lutz, and D. M. Eigler. Science **262**, 218 (1993).
- ⁵ J. Lobo-Checa *et al.* Science **325**, 300 (2009).
- ⁶ M. Kulawik *et al.* Surf. Sci. **590**, 253 (2005).
- ⁷ J. Voit *et al.* Science **290**, 501 (2000).
- ⁸ J. D. Sau *et al.* Phys. Rev. Lett. **101**, 026804 (2008).
- ⁹ E. V. Chulkov *et al.* Chem. Rev **106**, 4160 (2006).
- ¹⁰ R. D. Kronig and W. G. Penney. Proc. R. Soc. A. **130**, 499 (1931).
- ¹¹ K. L. Mutolo *et al.* J.A.C.S. **128**, 8108 (2006).
- ¹² T. Takami, C. Carrizales, and K. W. Hipps. Surf. Sci. **603**, 3201 (2009).
- ¹³ J. Y. Grand *et al.* Surf. Sci. **366**, 403 (1996).
- ¹⁴ K. Manandhar *et al.* Surf. Sci. **601**, 3623 (2007).
- ¹⁵ I. Kroeger *et al.* New J. Phys. **12**, 83038 (2010).
- ¹⁶ C. Stadler *et al.* Nat. Phys. **5**, 153 (2009).
- ¹⁷ D. G. Oteyza *et al.* J. Chem. Phys. **133**, 214703 (2010).
- ¹⁸ Supporting Online Material.
- ¹⁹ M. Koini *et al.* Thin Solid Films **517**, 483 (2008).
- ²⁰ I. Bezel *et al.* J. Chem. Phys. **120**, 845 (2004).
- ²¹ A. Mugarza *et al.* Phys. Rev. B **66**, 245419 (2002).
- ²² P. Puschnig *et al.* Science **326**, 702 (2009).
- ²³ A. D. Miller *et al.* Science **297**, 1163 (2002).
- ²⁴ T. Fauster and W. Steinmann. *Electromagnetic Waves*, volume 2, chapter 8 (Elsevier, Amsterdam) (1994).
- ²⁵ X. Zhu and C. Lindstrom. Chem. Rev. **106**, 4281 (2006).
- ²⁶ J. E. Ortega *et al.* Phys. Rev. B **65**, 165413 (2002).
- ²⁷ R. Stiufiuc *et al.* Phys. Rev. B **81**, 045421 (2010).
- ²⁸ A. Mayer. Phys. Rev. E **74**, 046708 (2006).
- ²⁹ J. Lei *et al.* Phys. Rev. B **63**, 045408 (2001).
- ³⁰ T. Miller, W. E. McMahon, and T. C. Chiang. Phys. Rev. Lett. **77**, 1167 (1996).
- ³¹ P. J. Feibelman and D. E. Eastman. Phys. Rev. B **10**, 4932 (1974).
- ³² A. Hotzel, M. Wolf, and J. Gauyacq. J. Phys. Chem. B **104**, 8438 (2000).
- ³³ S. Sachs *et al.* J. Chem. Phys. **131**, 144701 (2009).
- ³⁴ M. Shibuta *et al.* Phys. Rev. B **81**, 115426 (2010).
- ³⁵ R. C. Hatch, D. L. Huber, and H. Höchst. Phys. Rev. Lett. **104**, 047601 (2010).